Available online at www.sciencedirect.com

SciVerse ScienceDirect

Acta Materialia 61 (2013) 1739–1747

Acta MATERIALIA

www.elsevier.com/locate/actamat

Self-limited grain growth, dielectric, leakage and ferroelectric properties of nanocrystalline $BiFeO_3$ thin films by chemical solution deposition

Xianwu Tang, Xuebin Zhu *, Jianming Dai, Yuping Sun

Key Laboratory of Materials Physics, Institute of Solid State Physics, Chinese Academy of Sciences, Hefei 230031, People's Republic of China

Received 19 June 2012; received in revised form 20 November 2012; accepted 27 November 2012
Available online 21 December 2012

Abstract

In this study, the growth mechanism of nanocrystalline $BiFeO_3/Pt/Ti/SiO_2/Si$ thin films by chemical solution deposition has been investigated through isothermal annealing, and the dielectric, leakage and ferroelectric properties have also been studied in detail. The derived thin films show self-limited grain growth, which can be described well by a relaxation model, and the microstrain evolution follows exponential decay behavior. The dielectric constant and the loss behaviors have been investigated, and different contributions are expected for different thin films. The leakage current density behavior shows that conduction mechanisms are dominant, with the ohmic mechanism, the space-charge-limited current mechanism and the Fowler–Nordheim tunneling mechanism in low, middle and high electric fields, respectively. The behaviors of the ferroelectric coercive field and the polarization have also been investigated and found to be dominated by different factors for different samples. The results will provide an instructive route to optimize $BiFeO_3$-based thin films grown using the chemical solution deposition method.

Keywords: $BiFeO_3$; Grain growth; Dielectric; Leakage; Ferroelectric

1. Introduction

Multiferroic materials, which exhibit the coexistence of at least two ferroic properties (ferroelectric, ferromagnetic or ferroelastic), have been studied extensively due to both their rich physics and their wide potential applications [1,2]. Due to its high ferroelectric Curie temperature (1100 K), as well as its high magnetic Neél temperature (640 K), $BiFeO_3$ (BFO) has attracted tremendous attention as a very important multiferroic single-phase material [3–5]. Although intensive works have been carried out on BFO ceramics since 1960, it is difficult to prepare pure, dense and highly resistive ceramics due to the narrow growth window, which results in low polarization and magnetization at room temperature [6,7].

In 2003, Wang et al. [1] prepared BFO thin films with high remanent polarization and strong ferromagnetism at room temperature, and this has revived the investigation of BFO. Up to now, various methods have been used to prepare BFO thin films and to optimize their properties [8–16]. Among these methods, chemical solution deposition (CSD) is widely used due to its low cost, precise control of the stoichiometry, ability to achieve atomic-scale mixing and easy processing of large-area thin films [17,18].

Although there have been many recent investigations of BFO thin films grown by CSD, the processing parameters are not quite the same, which results in obvious differences in microstructures as well as physical properties [13,14,19,20]. It is suggested that the distinct differences are inherited from different microstructures, grain size/crystallite size, etc., which are needed to establish the relationships between processing, microstructure and

* Corresponding author. Tel.: +86 5515591439; fax: +86 5515591434.
E-mail address: xbzhu@issp.ac.cn (X. Zhu).

1359-6454/$36.00
http://dx.doi.org/10.1016/j.actamat.2012.11.048

properties. In general, the CSD-derived BFO thin films are nanocrystalline [15,16] and it is found that the grain growth of nanostructured material is different from that of conventional materials [21–23]. Although several grain-growth modes have been proposed to elucidate the grain-growth mechanisms in nanocrystalline thin films, few reports have focused on the grain-growth mechanism of BFO materials, which is essential for optimizing the BFO thin films.

In this paper, grain growth of CSD-derived BFO thin films has been investigated by isothermal annealing. The BFO thin films show self-limited grain growth that can be well described by the relaxation model. The dielectric, leakage and ferroelectric properties have been investigated systematically. The results will elucidate the differences in the microstructures as well as the properties for the CSD-derived BFO thin films, and will provide an instructive route to optimize such BFO-based thin films.

2. Experimental

BFO thin films were prepared by the CSD method as in our previous reports [15,16]. A 3 mol.% excess amount of bismuth nitrate pentahydrate was used to compensate the bismuth loss during processing. The final concentration of the solution was adjusted to 0.3 M. Thin films were deposited on Pt/Ti/SiO_2/Si (100) substrates by spin coating. The BFO thin films were annealed at different temperatures (475, 500, 525 and 550 °C) with different dwell times (5, 10, 20, 40, 60, 120, 240, 480 and 720 min) in a nitrogen atmosphere. Here, the thin films annealed at 475, 500, 525 and 550 °C are denoted as S475, S500, S525 and S550, respectively. For all the thin films, the thickness is ~560 nm, as determined by cross-sectional field-emission scanning electronic microscopy.

X-ray diffraction (XRD) using a Philips X'pert Pro diffractormeter with Cu Kα radiation was used to check the crystallization quality. Field-emission scanning electronic microscopy (FEI Sirion 200 type, FEI, Hillsboro, OR) was used to detect the thin film thickness and surface morphology. The sizes of crystallite were checked by transmission electron microscopy (TEM) inspection (JEM-2010, JEOL Ltd., Japan). Top Au electrodes 0.2 mm in diameter were deposited by sputtering, with small ion sputtering (SBC-12, KYKY, Beijing) onto the surface of BFO layer through a shadow mask. The dielectric response was investigated within the frequency range of 0 Hz–1 MHz with a driving voltage of 0.1 V by a precision inductance, capacitance, resistance meter (TH2828/A/S, Tonghui Electronic Co., Ltd., Changzhou). The ferroelectric and leakage properties as well as pulsed polarization positive-up, negative-down (PUND) measurement at a pulse width of 0.05 ms and delay time of 1 s were investigated using a Sawyer–Tower circuit attached to a computer-controlled standardized ferroelectric test system (Radiant Precision Premier II).

3. Results and discussion

3.1. Grain-growth kinetics

The XRD results show that all derived thin films are randomly oriented without parasitic phases. The average crystallite size was calculated through the three intense (001), (110) and (−110) peaks using the Scherrer equation, and all peaks were fitted by a Lorentz function. A silicon standard was used to account for the instrumental broadening. The Scherrer equation is only valid if there is no strain broadening, i.e. no local disorder associated with the microstrain. The microstrain estimations presented later suggest that this condition is an acceptable approximation, which is the same as a previous report about CeO_2/Ni thin films [24]. Additionally, TEM observation (not shown here) confirms that the crystallite size estimated by the Scherrer equation is acceptably exact. The derived crystallite size as a function of dwell time is shown in

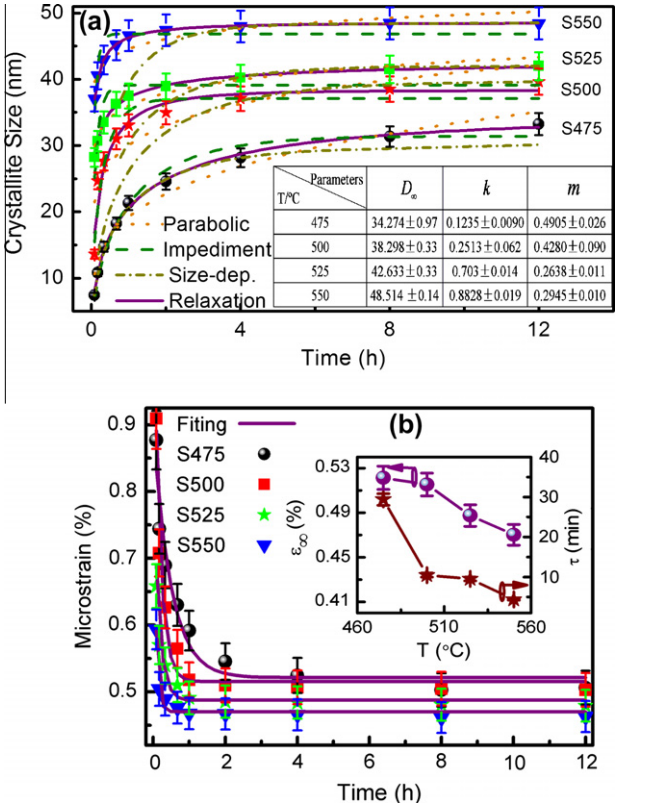

Fig. 1. (a) Evolution of crystallite size. Dotted lines: general parabolic model, dashed lines: standard impediment model, short dash-dotted lines: size-dependent impediment model, and solid lines: relaxation model. Estimated parameters by relaxation model fitting are shown in the inset. The error bars for crystallite size are estimated by applying error propagation rules to the Scherrer equation. (b) Microstrain dependence on annealing time with fits to the exponential decay function of microstrain. Variations of the deduced residual microstrain and relaxation time with annealing temperature are shown in the inset. The error bars of the microstrain are estimated by applying error propagation rules to the tangent formula.

Fig. 1a. It is clear that the higher the temperature is, the larger the crystallite size will be for a constant dwell time. For each annealing temperature, the crystallite initially grows rapidly within the first 60 min and then tends slowly towards a limiting value, which is similar to what has been previously reported [21–23].

Currently, four models have been applied to analyze the grain-growth kinetics, including the parabolic grain-growth model [25], the impediment grain-growth model [26], the size-dependent impediment grain-growth model [27] and the relaxation grain-growth model [28]. In order to analyze the grain-growth kinetics, all four grain-growth models have been used to fit the results. As shown in Fig. 1a, it is obvious that only the relaxation model is satisfied. The obtained parameters using the relaxation model, as described by Eq. (1), are shown in the inset of Fig. 1a. The limiting crystallite size and the rate constant k are enhanced, while the relaxation order m is suppressed with increasing annealing temperature, as in previous reports [29,30]. The size of the nanocrystals is significantly affected by the interface component between different grains. The microstructure of the BFO grain interface will be changed with the dwell time due to the enhanced diffusion and/or volatility of the bismuth at grain boundaries, which will lead to the rearrangement of grain bond lengths and/or angles near the BFO grain interfaces due to structural relaxation:

$$D(t) - D_0 = (D_\infty - D_0)(1 - \exp(-kt^m) \quad (1)$$

where k is the rate constant, m is the relaxation order, $D(t)$ is the average grain size after annealing time t and D_0 is the initial average grain size [28]. Since all thin films are crystallized from amorphous phases, the initial crystallite size D_0 is set reasonably to zero.

The averaged thin film microstrain comes from the local lattice distortions and/or the thermal expansion coefficient (TEC) mismatch between the BFO thin film and substrate, and it is also calculated using the three intense (0 0 1), (1 1 0) and (−1 1 0) peaks according to the tangent formula. As shown in Fig. 1b, the microstrain evolution can be well fitted by an exponential decay function [22]:

$$\varepsilon = \varepsilon_\infty + \varepsilon_s \exp(-t/\tau) \quad (2)$$

where ε_∞ is the residual microstrain ($\varepsilon_\infty = \varepsilon(t \to \infty)$), ε_s is a constant and τ is the relaxation time. From Fig. 1b, it is clear that the residual microstrain decreases quickly in the first 60 min and then tends to a saturated value, as in other reports [21,22]. It should be pointed out that the microstrain still exists, even when annealing involves high temperatures and long dwell times, which indicates that all the derived thin films are only partially relaxed. The annealing-temperature-dependent residual microstrain and relaxation time are shown in the inset of Fig. 1b. It is noteworthy that both the residual microstrain and the relaxation time decrease with increasing annealing temperature. Moreover, the relaxation time of the microstrain is comparable with that of the grain growth, which implies that the grain growth may be responsible for the microstrain relaxation, as commonly observed in CSD-derived thin films [31]. The large strain in thin films annealed for a short time at low temperature may be related to the presence of amorphous phases as well as the particularities of the thin films prepared by the CSD method. Small crystallites and poorly developed grains will lead to large microstrains in the derived thin films. With increasing annealing temperature and increasing dwell time, atom ordering in the crystal lattice and crystallization enhancement will induce the relaxation of microstrain, although the microstrain induced by the TEC mismatch [15,16,32] still exists.

3.2. Dielectric properties

The frequency dependent relative dielectric constant ($\varepsilon_r - f$) at room temperature has been measured within the frequency range of 0–1 MHz. To give a clear picture, the evolution of the dielectric constant measured at 1 MHz with annealing dwell time is shown in Fig. 2a. For each isothermal annealing temperature, the ε_r initially increases rapidly and then approaches a saturated value.

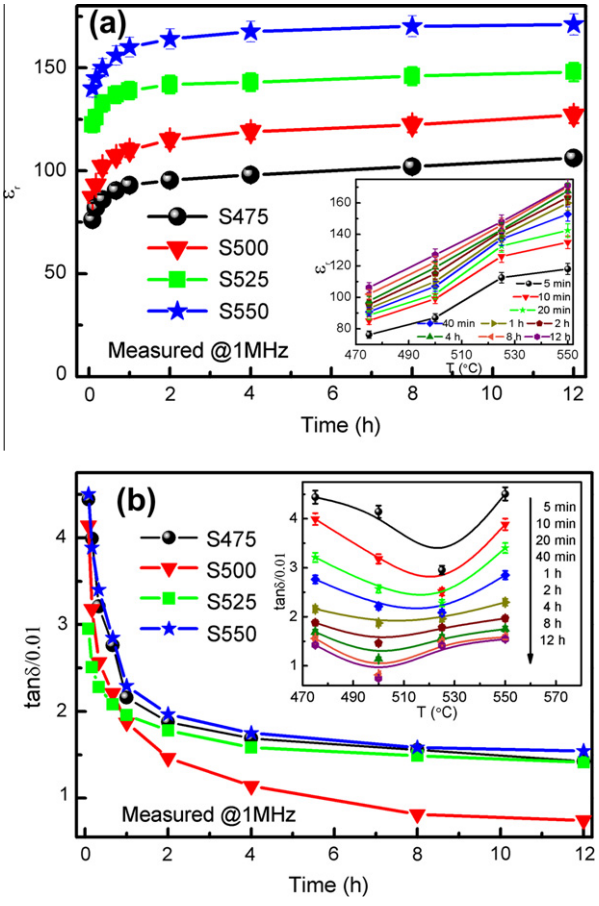

Fig. 2. Dependence of the room temperature relative dielectric constant (a) and loss measured (b) at 1 MHz. Evolution of the dielectric constant and the loss with the annealing temperature is shown in the inset of (a and b), respectively. The error bars of the dielectric constant and loss values are estimated based on the instrumental uncertainties.

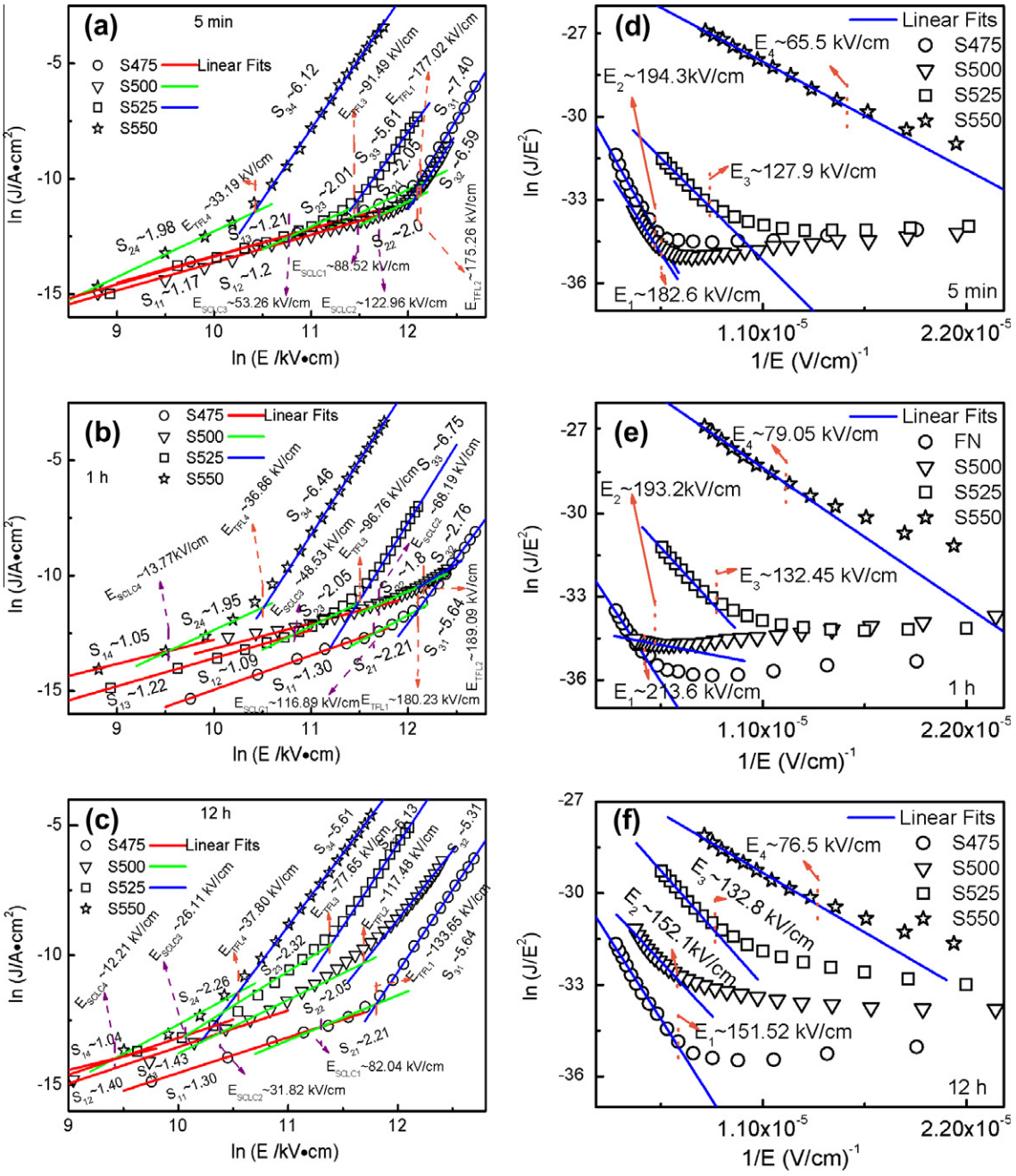

Fig. 3. Leakage current density fitted by SCLC (a–c) and FN tunneling (d–f) for several typical samples.

The evolution of ε_r with the annealing dwell time displays similar behavior to the crystallite size evolution. On the other hand, the dielectric constant increases almost linearly with the annealing temperature, as shown in the inset of Fig. 2a. It is well known that the dielectric permittivity of ferroelectric thin films consists of intrinsic and extrinsic contributions [33,34]. Among these intrinsic factors, the dielectric response of the individual domains [33] and the thin film orientation are the most important factors [34]. The grain/crystallite size as an extrinsic factor will also induce obvious effects on the dielectric response. Here, all the BFO thin films show subtle changes related to orientation, while the grain/crystallite size is increased with the annealing dwell time. An increase in grain/crystallite size will lead to a decrease in the internal stresses, which will favor the formation of 180° domains, resulting in an increased dielectric constant [34]. Additionally, the mechanical strain/stress in the thin films and the grain boundary pinning can influence the dielectric response of the domain wall motions and further affect the dielectric constant [33]. The strain, as shown in Fig. 1b, and the grain boundary density decrease with increasing annealing temperature and dwell time, which will enhance the dielectric constant.

The frequency dependent relative dielectric loss ($\tan\delta - f$) at room temperature was also measured within

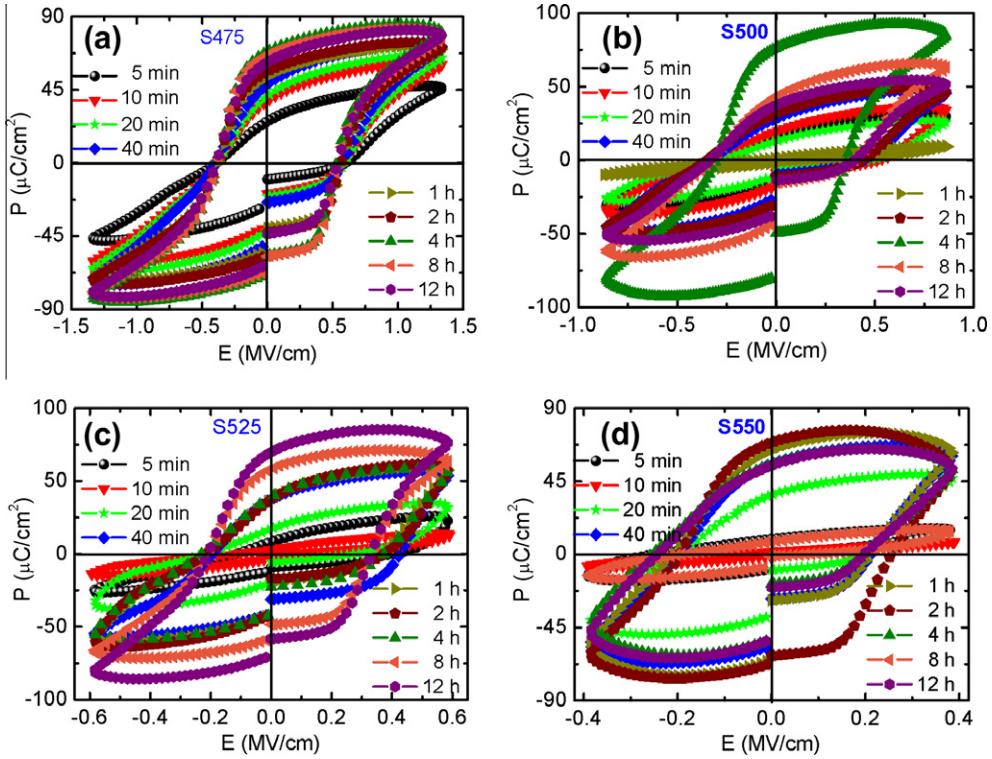

Fig. 4. Room temperature *P–E* hysteresis loops with the maximum applied electric field accepted by the BFO thin films annealed for 720 min: (a) S475, (b) S500, (c) S525 and (d) S550.

the frequency range of 0–1 MHz. The evolution of dielectric loss measured at 1 MHz with annealing dwell time is plotted in Fig. 2b. For each isothermal annealing temperature, tan δ initially decreases rapidly and then tends to saturate with increasing dwell time. The relationship between tan δ and the annealing temperature is shown in the inset of Fig. 2b, which shows a nonlinear relationship. The dielectric loss may be attributed to two factors [35]. One is the

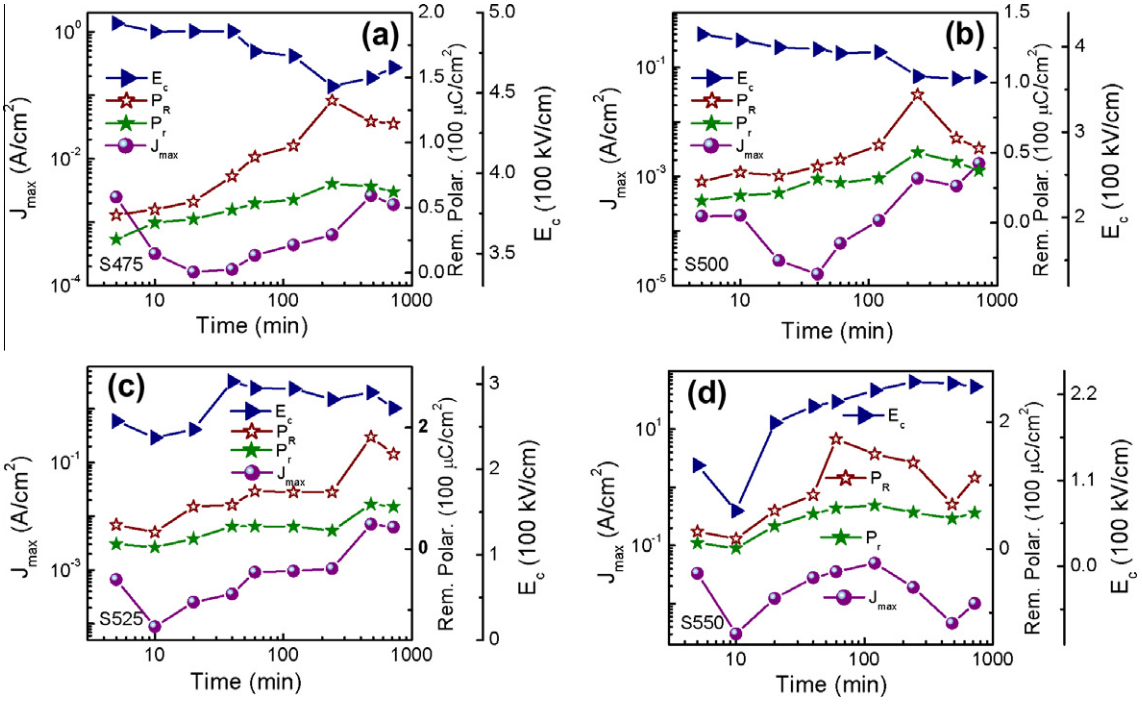

Fig. 5. Evolutions of J_{max}, E_c, P_r and P_R for all samples.

contribution of conduction to the dielectric loss, which comes from the conductive bismuth oxides, amorphous phases and oxygen vacancies that exist in the derived thin film. With the dwell time/annealing temperature increasing, the decrease in the amount of conductive bismuth oxides will lead to a decrease in the conductivity loss, which, in turn, reduces the dielectric loss. On the other hand, the decrease in amorphous phases, as well as the increase in oxygen vacancies with increasing dwell time/annealing temperature, will enhance the conductivity loss, which will give rise to enhancement of the dielectric loss. The other factor relates to the relaxation effects caused by the pinning at grain boundaries and high internal stress in the thin films. With increasing dwell time, the pinning effects on the polarization domain motion will obviously be suppressed due to the significant reduction in grain boundaries and microstrain, which will result in decreased dielectric loss. As mentioned above, the variation of $\tan\delta$ with annealing temperature may be caused by the combined effects of the decrease in bismuth oxides, as well as amorphous phases, and the increase in oxygen vacancies. However, the decrease in $\tan\delta$ with dwell time is mainly caused by the reduction of grain boundaries and microstrain.

3.3. Leakage properties

The leakage current density (J) at room temperature has been measured for all derived samples. To clarify the effects of the dwell time on J, the dependence of J measured at the positive maximum electric field (J_{max}) on the dwell time is shown in Fig. 5. The J_{max} values of samples S475, S500 and S525 decrease at first and then increase with the dwell time. For the S550 thin film, however, J_{max} decreases at first, then increases, and finally decreases again with the dwell time.

The amount of bismuth oxides decreases with increasing annealing temperature and longer dwell time, resulting in a decrease in J_{max}. On the other hand, the increase in oxygen vacancies due to the enhancement of crystallite size, as well as the decrease in grain boundaries, will lead to enhanced J_{max}. These two factors will lead to the J_{max} behavior seen in the S475, S500, and S525 samples. With further enhancement of the annealing temperature or prolongation of the dwell time, however, such as for the S550 thin film, the increase in bismuth deficiency (behaving like bismuth vacancy doping) will greatly compensate the oxygen vacancies and eliminate the bismuth oxides [10], which will lead to decreased J_{max} again.

To understand the conduction mechanisms in the derived thin films, several models have been tried to fit all the J–E curves. Firstly, the space-charge-limited current (SCLC) mechanism [36–38] was tested. $\ln(J)$ as a function of $\ln(E)$ for the thin films annealed for 5, 60 and 720 min, as typical results, is plotted in Fig. 3a–c, respectively. A power law relationship $\ln(J) \sim S\ln(E)$ is used to fit the curves, where S is the slope. All the curves can be well fitted by three straight lines. The fitting slope values S_{11}, S_{12}, S_{13} and S_{14} in low fields are ~1, and the slope values S_{21}, S_{22}, S_{23} and S_{24} are close to 2 in moderate fields, which agree well with the SCLC mechanism [36]. In higher electric fields, J shows an abrupt increase, with the slope values of S_{31}, S_{32}, S_{33}, and S_{34} all higher than 2. The abrupt increase in J may originate from the filling of the available traps due to high applied voltages, which can be explained by the trap-filled-limit (TFL) law [37]. The variations in the space-charge-limited electric field E_{SCLC} (at which there are conduction crossovers from ohmic to SCLC type), and the trap-filled-limit electric field denoted as E_{TFL} (at which J shows an abrupt increase with the dwell time) for each annealing temperature are shown in Table 1. The E_{SCLC} of S475 initially increases, and then decreases with longer dwell time. On the other hand, the E_{SCLC} for the other thin films decreases with the dwell time. According to the SCLC theory [38–40], the E_{SCLC} obeys $E_{SCLC} = 8qp_0d/9\theta_a\varepsilon_r\varepsilon_0$, - where q is the electron charge, p_0 is the density of thermally generated carriers, d is the thickness, θ_a is the ratio of free carrier density to total carrier density, which is in inverse proportion to the concentration of the traps, and ε_r is the relative permittivity. Thus, the reduction in the E_{SCLC} can be attributed to two factors. One is the increase in dielectric constant with the annealing temperature and the dwell time. The other is the decrease in grain boundaries, which act as traps and, in turn, increase the θ_a value. For the thin films annealed at 475 °C with a short dwell time, however, due to the presence of conductive bismuth oxides and amorphous phase, the thermally generated carrier concentration is high, which will lead to the initial increase in E_{SCLC}. The increase in E_{SCLC} for the thin films annealed at 550 °C with long dwell times, where variations in dielectric constant and the extent of grain boundaries have almost ceased, may be caused by the increased surface microcracks and bismuth vacancies due to the volatility of bismuth, which will lead to a decrease in the value of θ_a.

E_{TFL} for all the samples clearly increases at first and then decreases with increasing dwell time. The E_{TFL} is determined by $E_{TFL} = eN_td/2\varepsilon_r\varepsilon_0$ (where the unfilled traps density $N_t = H_a - p_t$, where H_a is the total trap density and p_t the concentration of carriers in filled traps) [40]. Based on the results for E_{TFL} and the measured dielectric constant, N_t is calculated as shown in Table 1. The variation in N_t with annealing temperature may result from the competition between the total trap density and the concentration of carriers in filled traps. The increase in oxygen vacancies due to the enhanced crystallite size, which act as one type of charge trapping center, will lead to an increase in H_a. On the other hand, the extent of grain boundaries will be decreased with the increasing annealing temperature, and p_t will be increased due to the increase in carrier injection or leakage current density, which will lead to the reduction of N_t. Similarly, the increase in N_t with dwell time can be also attributed to the decrease in grain boundaries, increase in oxygen vacancies and variations in carrier injection.

Table 1
The evolutions of E_{SCLC}, E_{TFL}, N_t and E_{FN}.

Time (min)	E_{SCLC} (kV/cm)	E_{TFL} (kV/cm)	N_t (10^{17})	E_{FN} (kV/cm)	Time (min)	E_{SCLC} (kV/cm)	E_{TFL} (kV/cm)	N_t (10^{17})	E_{FN} (kV/cm)
S475					*S500*				
5	84.8(8)	175.9(4)	2.4(4)	182.5(9)	5	122.9(6)	175.2(6)	2.8(1)	194.3(2)
10	103.8(9)	178.2(6)	2.4(2)	183.1(8)	10	103.1(6)	166.3(8)	2.8(2)	179.8(6)
20	123.6(2)	211.0(8)	2.7(8)	225.5(8)	20	94.6(6)	177.5(5)	3.2(7)	198.5(3)
40	112.7(5)	196.4(2)	3.2(9)	222.2(7)	40	91.4(9)	181.8(6)	3.5(6)	196.8(7)
60	112.5(3)	174.7(3)	3.0(4)	213.5(8)	60	68.1(7)	189.0(9)	3.8(1)	196.9(7)
120	96.5(7)	169.0(6)	2.8(5)	213.2(2)	120	67.5(3)	187.2(1)	3.8(8)	197.2(8)
240	102.6(4)	182.0(4)	2.7(9)	207.5(4)	240	48.5(3)	125.0(8)	2.6(8)	179.4(4)
480	80.1(2)	133.1(2)	2.2(7)	164.0(4)	480	55.9(8)	104.0(3)	2.3(1)	177.0(9)
720	91.9(5)	134.7(3)	2.5(8)	151.5(2)	720	31.8(2)	117.4(8)	2.7(1)	171.8(7)
S525					*S550*				
5	53.2(6)	91.4(9)	2.2(4)	127.9(3)	5	20.2(8)	33.1(9)	0.9(3)	65.4(8)
10	66.5(2)	126.2(5)	3.1(8)	145.9(9)	10	20.2(7)	49.6(3)	1.4(4)	73.6(7)
20	62.3(8)	111.5(2)	2.9(8)	136.9(7)	20	15.9(9)	40.4(9)	1.2(1)	69.5(4)
40	40.1(3)	104.9(2)	2.8(7)	132.7(5)	40	10.9(4)	41.6(1)	1.2(3)	78.4(3)
60	48.5(3)	96.7(6)	2.7(1)	132.4(5)	60	13.7(7)	36.8(6)	1.1(5)	79.0(5)
120	41.3(6)	88.4(3)	2.5(2)	122.5(5)	120	7.3(3)	34.8(9)	1.1(4)	85.1(4)
240	47.5(7)	76.4(2)	2.2(1)	111.3(3)	240	8.1(3)	31.2(6)	1.0(4)	83.3(3)
480	16.1(6)	67.8(5)	1.9(7)	138.3(1)	480	19.4(4)	41.7(7)	1.4(2)	54.0(5)
720	26.1(1)	77.6(5)	2.2(6)	139.0(8)	720	12.2(1)	37.8(2)	1.3(3)	76.5(1)

The interfacial layer between the thin film and the electrode cannot be avoided in the sandwich capacitance structure [41], and its effects on the leakage should be taken into account. The interface limited conduction mechanism caused by the injection of carriers into a ferroelectric layer from electrodes with tunneling through an interfacial energy barrier, which is Fowler–Nordheim (FN) tunneling, should also be present, and it can be expressed as $J_{FN} = CE^2 \exp\left(-\frac{D\varphi_i^{3/2}}{E}\right)$, where C and D are constants and ϕ_i is the potential barrier height. The onset electric field E_{FN} value for the FN tunneling is related to the potential barrier height of the interfacial layer [39]. Fig. 3d-f shows plots of $\ln(J/E^2)$ vs. $1/E$. A good linear fitting at high electric fields can be observed, which indicates the formation of a partial depletion layer between the thin film and the electrode [39]. As shown in Table 1, the reduction in E_{FN} with increasing annealing temperature suggests a decrease in the potential barrier height of the interfacial layer and an increase in J [42].

For the thin films annealed at low temperatures, such as S475 and S500, as well as the samples annealed at higher annealing temperatures but with short dwelling time, such as S525, J_{max} behaves in the same way as E_{FN} with respect to the annealing dwell time. The potential barrier height of the interfacial layer is related to the electric field, and the electric field can be described according to the two-capacitance model $E_d = \frac{P_f - J_i t}{\varepsilon_d}$, where P_f is the polarization of the ferroelectric layer, J_i is the injection current density through the interfacial layer, t is the measuring time and ε_d is the dielectric constant of the interfacial layer [43]. Furthermore, considering the contribution of leakage current density in the ferroelectric layer (J_f), the polarization of the ferroelectric layer (P_f) can be expressed as $P_f = P_f^0 + J_f t$, where P_f^0 is the intrinsic polarization of the ferroelectric layer. By substitution, this gives $E_d = \frac{P_f^0 + J_f t - J_i t}{\varepsilon_d} = \frac{P_f^0 + (J_f - J_i)t}{\varepsilon_d}$. At high electric fields, the injection current density is high. The resistivity of the thin films annealed at low temperatures or with short dwell times is very large, which will lead to a small value of J_f compared to the J_i within the measurement periods. This suggests that the leakage may be dominated by the injection current and that E_d is predominantly determined by the J_i. Thus, in this condition, the potential barrier height of the interfacial layer and the E_{FN} show similar behavior. For the thin films annealed at high temperatures, however, the leakage current density is very large, which will lead to a very strong injection close to the electrode. The insulating layer almost ceases to influence the potential barrier height [43]. The main contribution to the value of the leakage current density is the contribution from the ferroelectric film J_f. Thus, in this condition, the interfacial barrier height can be described as $E_d = \frac{P_f^0 + J_f t}{\varepsilon_d}$. Consequently, the value of E_d is dominated by the J_{max}, which results in both E_d and J_{max} displaying a similar tendency with the dwell time.

3.4. Ferroelectric properties

Fig. 4 presents the evolution of the polarization for the derived thin films. In fact, the thin films with short dwell time do not show good ferroelectric hysteresis loops, even with the maximum applied electric field accepted by the thin films annealed for 720 min at each temperature, which show hysteresis loops under higher fields (not shown here). Regardless of the annealing temperature, the longer the

dwell time is, the lower the applied maximum electric field that is needed to obtain a good ferroelectric hysteresis loop. Similarly, the higher the annealing temperature is, the lower the applied maximum electric field that is needed.

The dwell time dependence of the remanent polarization (P_r, defined as the average polarization at zero electric field) and the coercive field (E_c, defined as the average electric field at zero polarization) are presented in Fig. 5. The remanent polarization P_R obtained from PUND measurements is also shown in Fig. 5, which shows the same tendency as P_r. E_c for the thin films annealed at lower temperature is obviously higher than for the thin films annealed at higher temperature. It is well known that the crystallite size of a ferroelectric should have direct and remarkable effects on the ferroelectric properties [34]. The reported single-domain width of the BFO thin films ranges from 6 nm to 30 nm [11], which is coincident with the crystallite size of our derived thin films (in the range of 7–48 nm). Thus, the BFO thin films annealed at low temperatures are composed of small nanometer-sized grains, which can be characterized as predominantly single-domain grains. As the annealing temperature is increased, the grains are coarsened and can then be considered as multidomain grains. The single-domain grains are stable, and it is difficult to form new domains (nucleation) under an external electric field [44], so that the single-domain grains will show larger E_c than the multidomain grains. Moreover, the pinning of domain wall motion, which results from decreases in amorphous phase, grain boundaries and strains, will be reduced with increasing annealing temperature, resulting in decreased E_c.

Additionally, for the thin films annealed at low temperature, such as samples S475 and S500, the value of E_c decreases and P_r (P_R) increases dramatically in the first 240 min, after which E_c increases and P_r (P_R) decreases slowly with increasing dwell time, respectively. The decrease in the E_c values of the S475 and S500 thin films with the dwell time can be also attributed to the increase in multidomain grains and the reduction in the pinning of domain wall motion, as discussed above. On the other hand, for the thin films annealed at high temperature, such as samples S525 and S550, both E_c and P_r (P_R), except for the thin films annealed for 5 min, increase abruptly at the beginning of the dwell time, and then decrease slowly with increasing dwell time. For these thin films, the grain size is increased, and the grain boundaries and the microstrain are decreased with increasing dwell time, while E_c is increased with the dwell time, which suggest that other reasons should be considered. Actually, the interfacial layer that exists between the thin film and the electrode cannot be avoided in the sandwich capacitance structure [41]. The states in the vicinity of the electrodes are very crucial for the E_c value in the ferroelectric hysteresis loops [45]. The charges at the interface may create an electrical field, which opposes the ferroelectric switching for the subsequent phase in which the applied field is increasing. This effect will give rise to an increase in E_c in the sandwich structure. As Tagantsev reported [43], the E_c due to the existence of an interfacial layer can be described with different behaviors based on the relationship of the maximal polarization (P_m) to $\varepsilon_i \cdot E_{th}$ (ε_i is the dielectric constant of the interfacial layer and E_{th} is the threshold field in the interfacial layer, which is related to the leakage current). When $P_m < \varepsilon_i \cdot E_{th}$, corresponding to the low leakage state, the measured coercive field $E_c = E_{c0}$ (E_{c0} is the intrinsic coercive field in the BFO layer). So the decrease in the E_c values of the thin films S475 and S500 is caused by the decrease of grain size and the decreases of grain boundaries and microstrains. When the leakage current density is large, P_m may satisfy the relationship $2\varepsilon_i \cdot E_{th} > P_m > \varepsilon_i \cdot E_{th}$, and in turn, the coercive field $E_c = E_{c0} + t_i \cdot (P_m - \varepsilon_i \cdot E_{th})/\varepsilon_i(d - t_i)$, where t_i and d are the thicknesses of the interfacial layer and the thin film, respectively. Based on this equation, the increase in the P_m value with the dwell time will lead to the enhancement of the coercive field. If the annealing is further prolonged, the value of P_m, like the value of P_r, decreases with the dwell time, leading to a reduction in E_c. So the variation in E_c for the thin films S525 and S550, as well as the long-annealed S475 and S500, can be attributed to the effects of the interface layer and the leakage.

As for the relationship between the P_r (P_R) and the dwell time, two factors should be considered. One is the variation in multidomain grains and domain wall motion. On the other hand, the contribution of leakage current should be considered. The contribution of leakage current cannot be avoided in measurements of ferroelectric hysteresis loops [41], and the obtained remanent polarization can be characterized as $P_r = Q/2A = P_r^0 + Jt$ (Q is the switched charge). It can be seen that the measured polarization is proportional to the leakage current density. From Fig. 5, it is seen that the P_r (P_R) behaves in the same way as the leakage current with respect to the dwell time, except for the thin films annealed with short dwell times and at low temperatures. This suggests that the electrical conductivity makes a significant contribution to the polarization in the thin films with high leakage.

4. Summary and conclusions

Polycrystalline $BiFeO_3$ thin films are prepared on Pt/Ti/SiO_2/Si substrates by chemical solution deposition. It is observed that the derived $BiFeO_3$ thin films are nanocrystalline. The growth mechanism has been investigated by isothermal annealing. The crystallite size grows rapidly while the microstrain decreases quickly within the first hour, and then tends slowly to saturated values with further annealing dwell time, which suggest self-limited grain growth in nanocrystalline $BiFeO_3$ thin films. The grain growth can be well described by the relaxation model and the microstrain evolution follows exponential decay behavior.

For each isothermal annealing temperature, the dielectric constant and loss increases and decreases rapidly

within the initial hour, respectively, and then tends slowly to saturated values with further annealing dwell time, which is similar to the crystallite size and microstrain evolution, respectively. The evolution of dielectric constant is dominantly influenced by grain size effects as well as pinning effects of strain/stress and grain boundary, while the dielectric loss is dominantly influenced by different contributions of conduction and the relaxation effects.

The leakage current density decreases first and then increases with dwell time for low temperature annealed samples, while for high temperature annealed samples the leakage current density decreases first and then increases and finally decreases again. The behaviors are attributed to the variation of composition with annealing. The leakage current density shows that the conduction mechanisms are dominant, with the ohmic mechanism, the space-charge-limited current mechanism and the Fowler–Nordheim tunneling mechanism predominant in low, middle and high electric fields, respectively.

The behavior of the ferroelectric coercive field, as well as that of the polarization, is investigated. The coercive field is decreased with increasing annealing temperature due to grain size effects. The larger coercive field for low temperature annealed samples is attributed to the single-domain effects, while for the higher temperature annealed samples interface layer and leakage effects should be considered. As for the polarization, the variation in multidomain grains and domain wall motion as well as leakage effects should be considered.

The results will give a clear picture of the differences in microstructure as well as properties in CSD-derived BFO-based thin films, and provide an instructive route to optimize the properties of BFO-based thin films using the chemical solution deposition method.

Acknowledgements

This work was supported by the Director's Fund under Contract No. Y14N381323 of Hefei Institutes of Physical Science, Chinese Academy of Sciences and National Science Foundation of China under Contract Nos. 11204316, 50802096. We would like to thank Dr Tania M. Silver at University of Wollongong for English improvement and Professor Li Chen at Institute of Solid State Physics, Chinese Academy of Sciences for helpful discussion about XRD results.

References

[1] Wang JL, Neaton JB, Zheng H, Nagarajan V, Ogale SB, et al. Science 2003;299:1719.
[2] Thomas R, Scott JF, Bose DN, Katiyar RS. J Phys Condens Matter 2010;22:3201.
[3] Roginskaya YE, Venevtsev YN, Fedulov SA, et al. Sov Phys Crystallogr 1966;23:47.
[4] Kiselev SV, Kshnyakina AN, Ozerov RP, et al. Sov Phys Solid State 1964;5:2425.
[5] Kubel F, Schmid H. Acta Crystallogr Sect B Struct Sci 1990;46:698.
[6] Catalan G, Scott JF. Adv Mater 2009;21:2463.
[7] Smolensky GA, Isupov VA, Agronovskaya AI. Sov Phys Solid State 1959;1:150.
[8] Zheng RY, Gao XS, Zhou ZH, Wang J. J Appl Phys 2007;101:054104.
[9] Cheng ZX, Zhao HY, Du Y, Kimura H, Ozawa K, Wang XL. Scr Mater 2011;65:249.
[10] You L, Chua NT, Yao K, Chen L, Wang JL. Phys Rev B 2009;80:024105.
[11] Qi YJ, Chen ZH, Huang CW, Wang LH, et al. J Appl Phys 2012;111:104117.
[12] Singh SK, Maruyama K, Ishiwara H. Integr Ferroelectr 2008;98:83.
[13] Nanuma H, Okamura S. J Appl Phys 2007;101(09):M103.
[14] Singh SK, Ishiwara H, Maruyama K. J Appl Phys 2006;100:064102.
[15] Tang XW, Dai JM, Zhu XB, et al. J Am Ceram Soc 2010;93:1682.
[16] Tang XW, Dai JM, Zhu XB, et al. J Am Ceram Soc 2012;95:538.
[17] Schwartz RW. Chem Mater 1997;9:2325.
[18] Zarzycki J. J Sol–Gel Sci Technol 1997;8:17.
[19] Nakamura Y, Nakamura S, Okuyama M. Jpn J Appl Phys 2008;47:9.
[20] Gonzalez AHM, Simões AZ, Cavalcante LS, et al. Appl Phys Lett 2007;90:052906.
[21] Mihalache V, Pasuk I. Acta Mater 2011;59:4875.
[22] Rupp JLM, Infortuna A, Gauckler LJ. Acta Mater 2006;54:1721.
[23] Inham B, Linklater R, Kemmitt T. J Phys Chem C 2011;115:21034.
[24] Mihalache V, Pasuk I. Acta Mater 2011;59:5875.
[25] Burke JE, Turnbull D. Prog Metal Phys 1952;3:220.
[26] Grey EA, Higgins GT. Acta Metall 1973;21:309.
[27] Michels A, Krill CE, Ehrhardt H, Birringer R, Wu DT. Acta Mater 1999;47:2143.
[28] Mazurin OV. J Non-Cryst Solids 1977;25:129.
[29] Lai JKL, Shek CH, Lin GM. Scr Mater 2003;49:441.
[30] Chen ZW, Shek CH, Lai JKL. Appl Phys A 2005;80:703.
[31] Schwartz R, Schneller T, Waser R. CR Chim 2004;7:433.
[32] Chen HS, Krause JT, Sigety EA. J Non-Cryst Solids 1974;13:321.
[33] Xu F, McKinstry ST, Ren W, Xu BM, Xie ZL, Hemker KJ. J Appl Phys 2001;89:1336.
[34] Pérez de la Cruz J, Joanni E, Vilarinho PM, Kholkin AL. J Appl Phys 2010;108:114106.
[35] Sirdeshmukh DB, Sirdeshmukh L, Subhadra KG. Micro- and Macro-Properties of Solids: Thermal, Mechanical and Dielectric Properties. New York: Springer; 2006.
[36] Wang C, Takahashi M, Fujino H, Zhao X, Kume E, et al. J Appl Phys 2006;99:054104.
[37] Rose A. Phys Rev 1955;97:1538.
[38] Qi X, Dho J, Tomov R, Blamire MG, Driscoll JLM. Appl Phys Lett 2005;86:062903.
[39] Kao KC. Dielectric Phenomena in Solids. San Diego, CA: Elsevier/Academic Press; 2004.
[40] Sze SM, Ng KK. Physics of Semiconductor Devices. 3rd ed. New York: Wiley; 2007.
[41] Dawber M, Rabe KM, Scott JF. Rev Mod Phys 2005;77:1083.
[42] Yang F, Lai MO, Liu L, Zhu TJ. J Phys D Appl Phys 2011;44:435302.
[43] Tagantsev AK, Gerra G. J Appl Phys 2006;100:051607.
[44] Ren SB, Lu CJ, Liu JS, Shen HM, Wang YN. Phys Rev B 1996;54:R14337.
[45] Cillessen JFM, Prins MWJ, Wolf RM. J Appl Phys 1997;81:2777.